ISSN: 2790-5209 Vol 3, No.1, 2025

A Framework of Aircraft Wing Design Optimization at Various Atmospheric Conditions

Yifei Chen [1, *], and Yixuan Zhang [1 ‡]

[1] University of Michigan, Ann Arbor, MI 48109

Graduate Student, Department of Aerospace Engineering, AIAA Student Member

*Corresponding Author

‡ Co-first authors, listed alphabetically by last name

Abstract

This study introduces a gradient-based optimization framework for aircraft wing design tailored to varying atmospheric conditions. The optimization process incorporates key aerodynamic and structural considerations, including lift, drag, air density, and bending stress constraints, within a Multidisciplinary Design Optimization (MDO) framework. The design variables—wingspan and chord length—are optimized to minimize operational power while maintaining structural integrity. A BFGS gradient-based optimizer with a backtracking line search algorithm was selected after evaluating multiple optimization techniques, demonstrating superior efficiency and accuracy. Numerical results reveal that constrained designs favor reduced wingspan and increased chord length, preserving aerodynamic and structural performance compared to unconstrained solutions. Additionally, the study highlights the inverse relationship between wing area and pressure levels as a critical factor for optimal wing design. Given the dependency of air density and dynamic pressure on altitude, the framework offers flexibility to adapt designs for diverse environmental conditions. This approach provides an efficient and validated solution for energy-efficient, structurally robust wing designs, with broad applicability in aerospace engineering.

Keywords

Aircraft Wing Design, Multidisciplinary Design Optimization (MDO), Optimization Algorithms, Optimization Framework, Low-fidelity Model, (Rarefied) Atmospheric Condition, Aerodynamics, BFGS Gradient-based Method, Structural Performance, Aerospace Engineering

Nomenclature

A = Reference area of the wing
A_{wetted} = Wetted area
b_{sec} = Cross-section width
C_D = Drag coefficient
C_L = Lift coefficient
C_f = Skin friction coefficient
c = Chord
D = Drag
D_f = Viscous drag
D_i = Induced Drag

e = Oswald efficiency factor
$f(x)$ = Rosenbrock function
η = Propulsive efficiency
η_{max} = Maximum propulsive efficiency
ρ = Air density
h_{sec} = Cross-section height
I = Moment of inertia
k = Form factor
n = Number of design variables
n_P = Population of design points
L = Lift
M = Moment
P = Power
Re = Reynolds number
s = Wingspan
s_j = Step of j
σ_{max} = Maximum bending stress
σ_{yield} = Yield stress
t_w = Web thickness
t_b = Flange thickness
T = Thrust
μ = Air dynamic viscosity
U = Free-stream velocity
$\overline{U}$ = Flight speed at peak propulsive efficiency
W = Cruise weight
W_0 = Structure and payload weight
W_{area} = Wing area dependent weight
x_j = Design variable of j

1. Background and Motivation

The design of aircraft wing geometry is determined by multiple factors, including aerodynamic properties, range and mission design, structural performance, engine placement, load distribution, mass properties, and subsystem installation. It is critical for aircraft engineers to discover an optimal wing design that balances the "profit and loss" of different factors. The concept of Multidisciplinary Design Optimization (MDO) is the application of numerical algorithms to solve an engineering design problem that involves more than one design discipline [1]. The MDO algorithm optimizes a formulated function with constraints and design variables and discovers an optimal design point based on a reasonable initial guess. There are a variety of research areas in aerospace engineering that may benefit from MDO. For instance, MDO is applied to optimize airbreathing hypersonic vehicles, and the result shows a dramatic 46% range increase compared to the initial design [2]. This paper focuses solely on the implementation of MDO in aircraft wing geometry designs, including both aerodynamic and aero-structural considerations.

According to previous studies [3, 4], variations in atmospheric conditions, particularly changes in air density, have a significant impact on the aerodynamic performance of aircraft. Optimized wing geometry, including wing area, wingspan, and chord dimensions, must be carefully adjusted to accommodate these changes. For instance, the atmospheric conditions at 30-km altitude exhibit drastically lower air density than those at sea level due to the rarefied environment. Table 1 provides a comparison of specific atmospheric parameters at sea level, 30-

km altitude on Earth, and conditions on Mars, respectively. The extreme reduction in air density at high altitudes presents substantial engineering challenges in designing a functional and flyable aircraft capable of performing under such conditions. One of the most critical challenges is the generation of sufficient lift, as low air density severely diminishes the aerodynamic performance. To counteract this, the design of the wing area must scale proportionally with the decrease in atmospheric density, ensuring sufficient lift generation to sustain flight. A fundamental approach to addressing this issue involves increasing the aircraft wing area, as a larger wing area allows for greater lift generation under rarefied conditions. However, continuously increasing the wing area introduces significant aero-structural challenges. Specifically, a longer wingspan combined with a thinner chord can result in substantial bending and shear stresses at the wing root due to large normal and axial forces. These stresses can compromise structural integrity and pose safety concerns. To address this, a bending stress constraint must be incorporated into the optimization process to ensure the structural feasibility and safety of the wing design. In this study, the objective function focuses on minimizing the required power for an aircraft, which is inherently correlated to the aerodynamic performance and the optimized wing geometry (wingspan and chord). A bending stress equation is introduced as a constraint to account for aero-structural considerations. Balancing aerodynamic efficiency and structural integrity, the optimization program delivers a safer, more practical wing design suitable for real-world applications under varying atmospheric conditions.

The works of Caros et al. [5] and Shapiro and Manela [6] offer innovative approaches for leveraging MDO solvers to address complex aircraft wing design challenges under rarefied atmospheric conditions. Inspired by these advancements, this study establishes the overarching objective of minimizing the aircraft's power requirement during flight as the primary objective function. The parameters within the power equation are intricately linked to the aerodynamic performance of the aircraft, both directly and indirectly, thereby playing a critical role in influencing the optimal wing geometry. By capturing the interdependencies between power consumption and aerodynamic efficiency, the optimization framework provides a robust and systematic approach for achieving efficient and practical wing designs in rarefied environments.

This study chose to minimize the required power for the aircraft in cruising flight by varying its wingspan and chord. There are three reasons for the optimization function selection. Firstly, reducing the power required in cruising flights decreases the propellant requirement for the flight, which allows the airliner to reduce the cost of jet fuel. Secondly, minimizing the required power increases the aircraft's mission range using the same amount of fuel. The airliner could operate the aircraft over a longer distance without concern about additional expenses. Thirdly, the airliners will be more profitable if the aircraft reduces its designed cruising power. In addition to the financial advantage of fuel-saving and better range, the airliners also save maintenance costs for engines, because their operating intensity is reduced since the required power is dropped.

When optimizing the design variables, wing structure, another discipline besides aerodynamics, is interrelated with the variables of wingspan and chord. The structural performance, such as bending and torsion resistance, determines the flight safety of an aircraft, which is the top priority of aviation. The reason to account for structural performance of the wing is to avoid safety issues, such as material fatigue, permanent damage, or even structural failure. Most aircraft wing design consists of a front and rare spar to resist loads and torsions. The dimensions of spars are designed based on the wing geometry. For example, the spar length is equal to the span, and the spar width is proportional to the length of the chord. Additionally, the placement of spars is also decided by the chord length, thus affecting the torsion resistance of the wing. Without the assistance of MDO, it will be an iterative process for aerodynamicists and structure engineers to size the wing

geometry to obtain the optimal aerodynamic performance while maintaining structural safety. However, with the powerful numerical tools of MDO, the program software is able to account for the wing's structural strength as constraints when optimizing toward a specific objective.

Property	Earth (Ground)	Mars (Ground)	Earth (30 km)
Gravity (m/s^2)	9.81	3.72	9.78
Density (kg/m^3)	1.225	0.0167	0.0177
Pressure (Pa)	101325	660	1150
Specific Heat Ratio	1.4	1.34	1.4

Table 1: Comparison of average characteristics of Earth and Mars' atmosphere [4].

2. Investigation on the Coupled Models

The investigation of coupled models is critical for analyzing and selecting the most appropriate and efficient optimization approach for a specific Multidisciplinary Design Optimization (MDO) problem. This study examines two classes of optimization methods for aircraft wing design: (1) gradient-free methods and (2) gradient-based methods. Each approach presents distinct advantages and limitations. Gradient-free optimization methods rely solely on objective function evaluations, without requiring derivatives or Hessians. This makes them straightforward to implement and advantageous for problems where gradient information is intractable or expensive to compute. However, their slow convergence rates, lower solution precision, and limitations in handling high-dimensional problems must be carefully evaluated in the context of the application. In contrast, gradient-based optimization methods utilize gradient information to efficiently navigate the search space, offering high precision, computational efficiency, and scalability for large-scale problems. Despite these strengths, their reliance on gradient availability and sensitivity to initial guesses introduces complexity, particularly for highly non-linear or non-convex optimization tasks. Ultimately, the choice of method depends on the specific problem characteristics and the trade-off between computational cost and optimization accuracy, emphasizing the importance of selecting an approach that aligns with the problem's requirements.

2.1. Analysis of Gradient-Free Methods

Two gradient-free algorithms are designed: the Nelder-Mead algorithm and the Real-Encoded Genetic algorithm. The simplex method of Nelder and Mead (NMs) is a deterministic, direct-search method that is among the most cited gradient-free methods. Genetic algorithms (GAs) are population-based evolutionary algorithms.

Table 2 elucidates the global optimum of the 2D Rosenbrock function obtained using five different methods. All five algorithms, encompassing both gradient-free and gradient-based approaches, converge nearly to the global optimum, which coincides with the exact solution, [1, 1]. The optimal function values achieved are all close to zero, the exact global optimum function value. Among these methods, the real-encoded genetic algorithm demonstrates the least relative error. In general, gradient-based methods incur lower computational expense than gradient-free methods, requiring fewer iterations to achieve convergence. Moreover, the gradient-based algorithms, such as BFGS, and the real-encoded genetic algorithm, a type of gradient-free method, consistently converge to the exact global optimum even in high-dimensional problems with up to 256 dimensions. In contrast, numerical results indicate that the two Nelder-Mead algorithms fail to converge to the global optimum when the problem dimension exceeds 16.

Figure 1 illustrates the convergence rates of the 2D Rosenbrock function for various algorithms, starting from the initial point [0, 0]. The results demonstrate that the gradient-based BFGS algorithms achieve convergence with the fewest iterations, highlighting their computational efficiency. Additionally, the real-encoded genetic algorithm exhibits superior accuracy, achieving solutions with minimal relative errors. In contrast, the Nelder-Mead (NM) algorithms are characterized by their simplicity and ease of implementation. The performance of the custom-implemented NM algorithm aligns closely with that of the off-the-shelf NM algorithm from SciPy, demonstrating consistent efficiency and accuracy across implementations.

Table 3 and Figure 2 present the relationship between the number of function evaluations for the Rosenbrock function and its dimensionality across various algorithms. The results indicate that the number of function evaluations increases proportionally with the dimensionality of the Rosenbrock function for all algorithms. Notably, all algorithms exhibit a positive correlation between iterations and dimensionality, with the exception of the Real-Encoded Genetic Algorithm, which demonstrates a relatively flat trend, highlighting its robustness to dimensional increases.

Table 2: 2D Rosenbrock Function Optimization with Five Different Methods

Method	x*	f (x*)	Iterations
Nelder-Mead	[0.99999985, 0.99999974]	$1.72527553714 \times 10^{-13}$	83
Real-Encoded Genetic	[1.00000000, 1.00000000]	$3.91002694915 \times 10^{-21}$	100
Off-the-Shelf NM	[1.00000439, 1.00001064]	$3.68617691518 \times 10^{-10}$	79
BFGS (FD)	[0.99999911, 0.99999821]	$8.06633167879 \times 10^{-13}$	20
BFGS (AG)	[0.99999913, 0.99999825]	$7.71728835661 \times 10^{-13}$	20

Table 3: Number of Function Calls with Dimension by Various Methods

Method	2D	4D	8D	16D	32D
Nelder-Mead Algorithm	83	290	1412	13158	237753
Real-Encoded Genetic Algorithm	100	100	100	100	100
Off-the-Shelf NM	79	245	1137	2525	5512
BFGS (Finite-Difference)	20	34	55	89	165
BFGS (Analytic Gradients)	20	34	55	92	164

The Nelder-Mead (NM) algorithm is based on a simplex. It is a geometric figure defined by a set of n + 1 points in the design space of n variables. The NM algorithm with fewer variables (n) will be non-functional when the problem is multidimensional. Increasing the design space of n variables solves the inaccuracy and non-convergence while applying the NM algorithm to higher-dimensional problems.

The first step of the simplex algorithm is to generate n + 1 points based on an initial guess for the design variables. For the displayed cases, the starting point (x_0) is set as [−1.2, 1.4], the edge length (l) of the simplex is set to 1, and the number of design variables (n) is set to 3. New points ($x^{(1)}$, $x^{(2)}$, $x^{(3)}$) for an equal-length-edge simplex are generated by adding steps (s_j) to each component of the initial point. Secondly, the simplex size tolerances and the function value standard deviation tolerances are defined to quantify the convergence of the simplex method. Thirdly, the order of simplex points is sorted from the lowest (best) to the highest f ($x^{(j)}$). New points are then required to be created. The Nelder-Mead (NM) algorithm performs five primary operations on the simplex to create a new one: reflection, expansion, outside contraction, inside contraction, and shrinking. Each iteration aims to replace the worst point with a better one to form a new simplex (the centroid, x_c). Each iteration always starts with

ISSN: 2790-5209 Vol 3, No.1, 2025

reflection, which generates a new point (reflection, x_r). If the reflected point is better than the best point, the search direction is considered good, and the simplex expansion is performed with α = 2. If the reflected point is between the second-worst and the worst point, the direction is deemed poor, and an outside contraction is performed ($\alpha = \frac{1}{2}$). If the reflected point is worse than the worst point, the NM algorithm applies an inside contraction instead ($\alpha = -\frac{1}{2}$). The last-resort operation is shrinking, performed when no point along the line connecting $x^{(n)}$ and x_c yields a better solution.

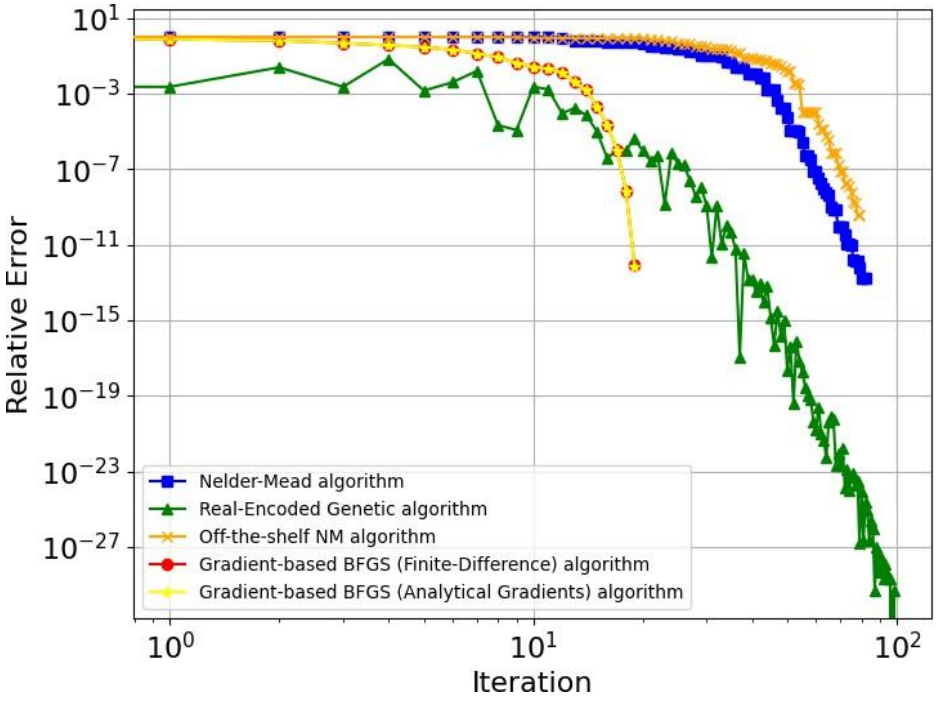

Fig. 1: Convergence rate of 2D Rosenbrock function with a starting point at [0, 0].

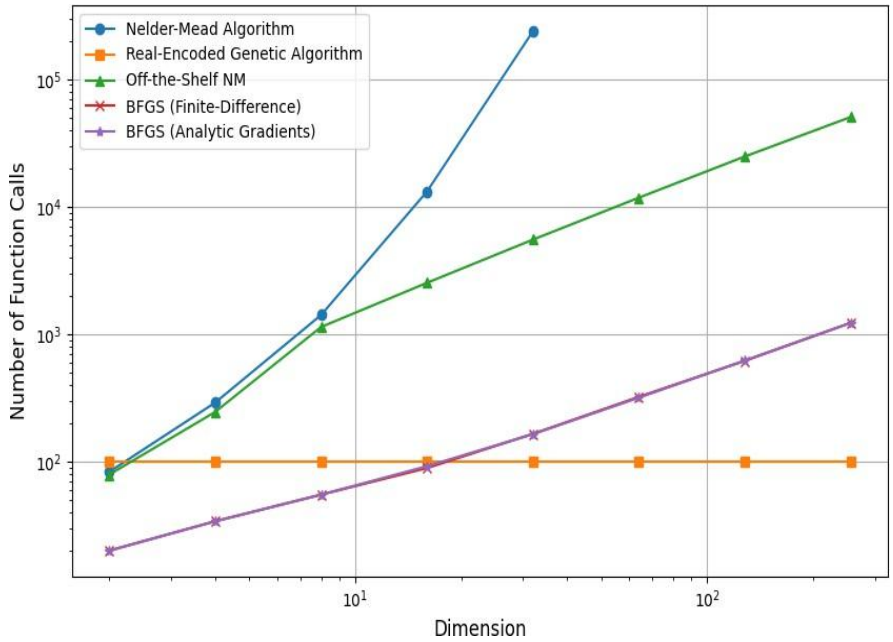

Fig. 2: Plot of function calls with dimension for different optimization methods.

ISSN: 2790-5209 Vol 3, No.1, 2025

The Real-Encoded Genetic Algorithm (GA) operates on a population of design points rather than a single starting point. In each GA iteration, referred to as a generation, a population of design points (n_p) is maintained, where each design is represented by a chromosome, and each design variable is represented as a gene. The iterative steps of the coded GA are inspired by biological reproduction and evolution, consisting of three main operations: (1) selection, (2) crossover, and (3) mutation. Genetic algorithms also employ different encoding methods for representing design variables, including binary-encoded and real-encoded approaches. This study uses the real-encoded genetic algorithm to define the design variables for further analysis.

For the real-encoded genetic algorithm, lower and upper bounds must be specified as part of the initial setup to constrain the range of the population generation. First, an initial random population is generated, followed by the evaluation of the objective function. A tournament selection process is applied during the selection step, where n_p points are paired randomly, and the best point from each pair is selected to join the mating pool. A linear crossover method is used during the crossover step, generating two or more offspring points along the line defined by the two parent points. Specifically, child 1 is computed as the average of the two parent points, while child 2 is determined by extrapolating in the direction of the "fitter" parent. Finally, mutation occurs with a small probability of p = 0.005, introducing random changes to some points in the population. Bound checking is necessary during mutation to ensure all mutated points remain within the predefined lower and upper limits.

2.2. Analysis of Gradient-Based Methods

An optimization solver integrating the BFGS direction search method with the Bracketing line search algorithm and the strong Wolfe conditions has been developed for evaluation. The objective is to identify an efficient optimizer suitable for the aircraft wing design application, based on a comprehensive comparison and selection process. The final choice of the direction search method and line search algorithm was made by evaluating the convergence rates of function iterations across two direction search methods and two line search methods, resulting in four distinct optimization systems. Table 3presents the successful application of the BFGS optimizer in solving the 2D Rosenbrock test problem, demonstrating its efficacy. As a result, the BFGS optimizer was validated and selected as the final optimization method for the application.

Newton's method is highly efficient due to its use of second-order information, which provides superior search directions. However, it has the significant drawback of requiring the Hessian matrix, which is challenging to compute analytically for complex objective functions in gradient-based optimization. Consequently, Newton's method is often impractical for such problems, making the Quasi-Newton method a viable alternative. The Quasi-Newton method addresses this limitation by approximating the Hessian matrix using first-order information (gradients), offering high computational efficiency compared to steepest descent and conjugate gradient methods. Quasi-Newton methods are typically robust and require fewer function evaluations, resulting in significant computational time savings. Unlike Newton's method, which may lack robustness and can terminate prematurely at local minima in some instances, Quasi-Newton methods iteratively build an approximation of the Hessian by utilizing the gradient at each step. These methods estimate curvature in the step direction and refine the Hessian approximation, enabling them to leverage a quadratic approximation of the objective function in combination with a line search algorithm.

Table 4: 2D Rosenbrock function optimization results with coupled different search directions and line search methods. The convergence tolerance is 1e-5.

Method	Search Direction	$f(x^*)$	x^*	Iterations	Function Calls
Gradient Descent	Backtracking	6.1319×10^{-11}	[0.99999218, 0.99998432]	10,916	21,084
	Bracketing/Pinpointing	1.0980×10^{-10}	[0.99998953, 0.99997902]	2,733	12,901
BFGS	Backtracking	1.2326×10^{-32}	[1.00000000, 1.00000000]	37	56
	Bracketing/Pinpointing	0.0	[1.00000000, 1.00000000]	42	565
BFGS Off-the-Shelf Optimization	-	2.5353×10^{-15}	[0.99999997, 0.99999995]	32	64

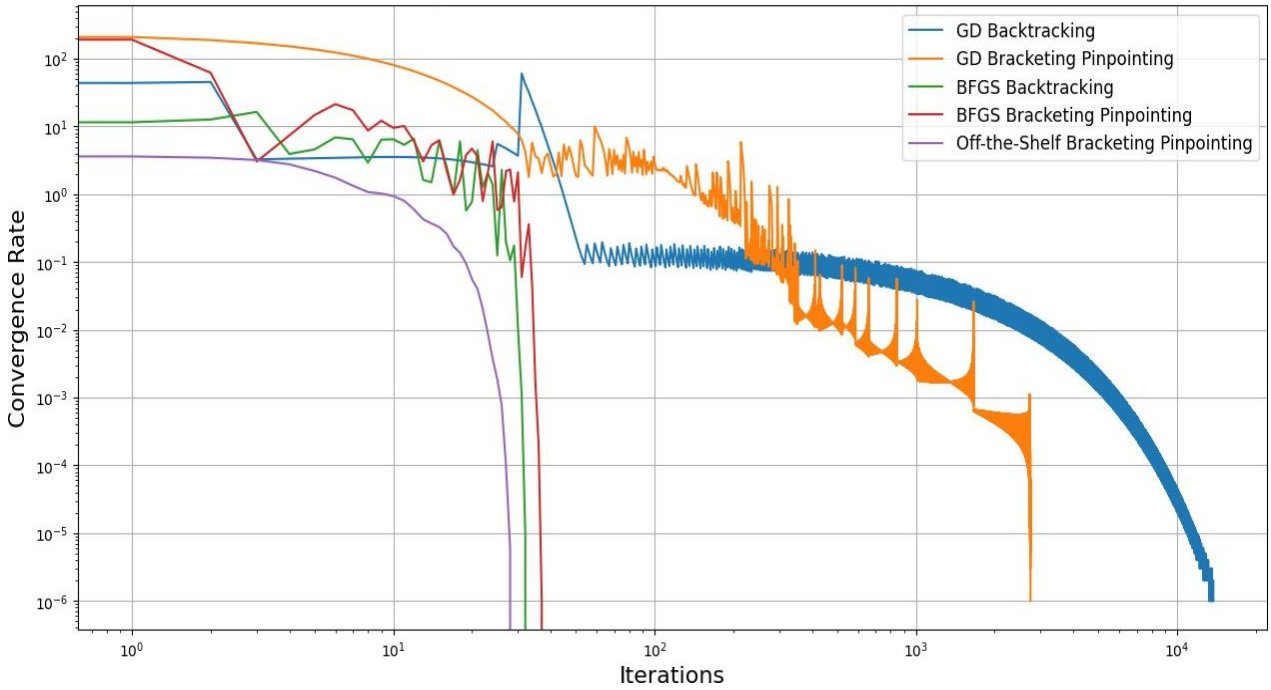

Fig. 3: Convergence rate with iteration for different optimization algorithms for solving the 2D Rosenbrock function.

According to Table 3, the most efficient and robust optimization solver is the BFGS method coupled with the Backtracking line search algorithm. This combination provides the most accu-rate estimation of the global minimum with the fewest function iterations compared to exact numerical solutions. Under identical convergence tolerances, the BFGS solver with Backtracking demonstrates greater computational efficiency than the off-the-shelf BFGS optimizer. The performance of various optimizers was evaluated using the 2D Rosenbrock function. As shown in Table 4, the Gradient Descent (GD) method, combined with either the Backtracking or Bracketing-Pinpointing line search algorithms, is significantly less efficient than the Quasi-Newton method. Specifically, solving the 2D Rosenbrock function requires 10,916 and 2,733 iterations for Gradient Descent when using the Backtracking and Bracketing -Pinpointing algorithms, respectively. In contrast, when paired with the same respective line search algorithms, the BFGS solver requires only 37 and 42 iterations. Thus, the BFGS solver coupled with the Backtracking line search algorithm emerges as the most efficient and accurate gradient-based optimization method. Moreover, it can outperform standard off-the-shelf optimization tools, such as Scipy minimize, for specific problem domains.

2.3. Final Decision of Utilized Optimizer in Applications

This study evaluated gradient-free and gradient-based optimization methods to determine their accuracy and efficiency. Gradient-free methods included Nelder-Mead (NM) and Real-Encoded Genetic Algorithm (GA), while gradient-based methods combined direction search techniques like BFGS and Gradient Descent with line search algorithms (e.g., Backtracking, Bracketing, and Pinpointing). Based on the results in Tables 3 and 4, the BFGS method with Backtracking line search was selected as the final optimizer for the aircraft wing design problem. This configuration demonstrated superior efficiency, robustness, and accuracy, outperforming alternative methods despite slightly higher iteration counts in specific quadratic cases. The advantages of its precision and computational efficiency far outweighed any minor drawbacks. Figures 1and 3 illustrate the BFGS optimizer's superior convergence rates on the Rosenbrock function, underscoring its effectiveness for this application. The selection was based on a thorough evaluation of convergence rates, iteration counts, and computational efficiency across the 2D Rosenbrock test case. Key observations from the investigation are as follows:

- **Performance on 2D Rosenbrock Function:**

  – BFGS coupled with Backtracking converged to the global minimum at a function value of approximately 1.2326×10^{-32} within 37 iterations and 56 function evaluations.

  – In contrast, Gradient Descent with Backtracking required 10,916 iterations and 21,084 function evaluations to converge, highlighting the inefficiency of gradient-only methods compared to Quasi-Newton approaches.

  – BFGS with Bracketing-Pinpointing also performed well but required more iterations (42) and function evaluations (565) than Backtracking.

- **Advantages of BFGS with Backtracking:**

  – **Efficiency:** The solver consistently required fewer iterations and function evaluations than gradient-only methods and even other Quasi-Newton configurations.

  – **Robustness:** BFGS with Backtracking maintained stable performance across different test functions, avoiding the pitfalls of local minima that can plague Newton-based methods.

  – **Accuracy:** The combination provided highly precise results, achieving global minimum values identical to exact solutions in numerical tests.

- **Limitations of Alternative Approaches:**

  – Newton's method, while theoretically efficient, was unsuitable due to the computational infeasibility of obtaining analytic Hessians for the application's complex objective functions.

  – Gradient-free and gradient-only methods like NM and GD were computationally expensive and inefficient, particularly for higher-dimensional problems, requiring significantly more iterations to converge.

Based on the findings, the BFGS method coupled with the Backtracking line search algorithm was selected as the final optimizer. This solver offers a superior balance of computational efficiency, robustness, and accuracy, making it ideal for solving the complex, high-dimensional optimization problems associated with the aircraft wing design application. As illustrated in

Figures 1 and 3, the convergence rates for BFGS with Backtracking outperform alternative methods, further reinforcing its suitability for the task. The final implementation leverages the strengths of the BFGS method and Backtracking line search, ensuring reliable and efficient optimization for the problem domain.

3. Methodology

The objective of the problem is to discover the optimal wingspan and chord under different atmospheric conditions. The wing geometry is determined by the span and chord, which is critical to compute aerodynamic forces, mass properties, and propulsive efficiency. The reference area and wetted area of the aircraft wing are defined in Equation 1.

$$A = bc, \qquad A_{\text{wet}} = 2.05\ A \tag{1}$$

According to Equation 2, the change in wing geometry impacts the aerodynamic forces acting on the aircraft, specifically lift and drag forces. These forces are used to calculate the aircraft dynamics, such as cruising speed and climb rate.

$$L = \frac{1}{2}\rho U^2 A C_L, \qquad D = \frac{1}{2}\rho U^2 A C_D \tag{2}$$

The aircraft is assumed to maintain a constant speed at its cruising altitude. Therefore, the magnitude of the lift force equals the aircraft's cruising weight, which could be estimated using Equation 3.

$$L = W = W_0 + W_{area} A \tag{3}$$

The total drag force acting on the aircraft has two major components: parasite (zero-lift) drag and drag due to lift [7]. These two components could be approximated using multiple methods. Still, this report implemented the skin-friction method to calculate the parasite drag and the Oswald span efficiency method to estimate the drag due to lift. Equation 4 calculates the skin friction coefficient using the Reynolds number. The parasite drag component D_f is estimated by Equation 5. The Oswald span efficiency method calculates the induced drag D_i in Equation 5 using the lift force and the Oswald efficiency factor e. Finally, the total drag on the aircraft is computed by adding the drag components.

$$C_f = \frac{0.074}{Re^{0.2}}, \qquad \text{where} \qquad Re = \frac{\rho U c}{\mu} \tag{4}$$

$$D_f = \frac{1}{2}\rho U^2 k C_f A_{wet},\ D_i = \frac{L^2}{1/2\rho U^2 \pi b^2 e}, \qquad D = D_f + D_i \tag{5}$$

One key component for computing engine power is the propulsive efficiency, which is usually estimated by a Gaussian model based on the maximum efficiency parameters. Equation 6 calculates the propulsive efficiency. Eventually, the aircraft propulsive power could be calculated by Equation 7, which is also the objective function of the problem formulation.

$$\eta = \eta_{max} \exp\left(\frac{-(U-\bar{U})^2}{2\sigma_{std}^2}\right) \tag{6}$$

$$f(b,c) = P = \frac{DU}{\eta} \tag{7}$$

Structural safety is another critical consideration when designing the aircraft wing geometry. When cruising at high altitude, the wing is often subjected to a bending moment and torsion due to the nonuniform distribution of lift on the surface of the wing. The front spar of the wing

structure is designed to withstand most of the bending moment, which needs to be constrained by a safety factor. Figure 4 shows an I-beam (also referred to as H section) which is usually selected as the front spar of the aircraft wing. The geometry of the beam cross-section is designed based on the wingspan and chord. In this study, it is assumed that the height and width of the I-beam are proportional to the chord, shown in Equation 8. Indicated in Equation 9, the web and flange thicknesses are kept constant to simplify the calculation.

$$h_{sec} = 0.1c, \qquad b_{sec} = 0.4c \tag{8}$$

$$t_w = t_b = 0.004\ m \tag{9}$$

A key variable to compute the bending moment is the moment of inertia, which is determined by the cross-section design of the I-beam. Equation 10 shows the method for approximating the moment of inertia of the wing spar.

$$I = \frac{h_{sec}^3}{12} t_w + \frac{b_{sec}}{6} t_b^3 + \frac{h_{sec}^2 b_{sec}}{2} t_b \tag{10}$$

We assume a uniform span-wise lift distribution, meaning the lift force could be considered a point force acting on the 12.5% span point from the root chord. Thus, the bending moment is calculated using Equation 11.

$$M = \frac{Lb}{8} \tag{11}$$

Equation 12 can be used to obtain the maximum bending stress on the spar with the bending moment. This term indicates the highest stress acting on the structure, which needs to be constrained within a designed range to avoid structural fatigue, permanent damage, or even failure.

$$\sigma_{max} = \frac{M h_{sec}}{2I} \tag{12}$$

The stress constraint is formulated as follows. The ultimate load and safety factors are assumed to be 2.5 and 1.5. The ultimate stress on the wing spar shall always be kept under the material yield stress with the consideration of a 1.5 safety factor, which is illustrated in Equation 13. The mathematical form of the constraint is shown in Equation 14.

$$ultimate\ load\ factor \times maximum\ stress \leq material\ yield\ stress\ with\ 1.5\ safety\ factor \tag{13}$$

$$2.5\ \sigma_{max} - \frac{\sigma_{yield}}{1.5} \leq 0 \tag{14}$$

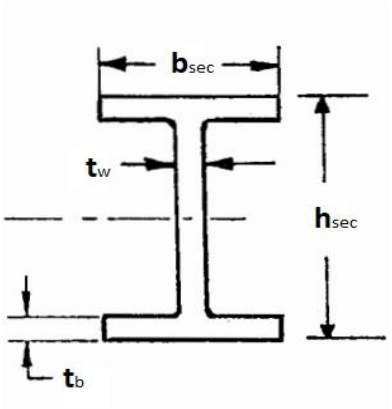

Fig. 4: Geometry of the front spar of the wing structure.

4. Optimization Problem Formulation

The optimization problem is the power optimization of a rectangular lifting-surface platform for which directly considers the viscous and induced drags and indirectly considers the lift. The optimization problem is formulated as follows:

$$\begin{aligned} &minimize && P(b,c) = \frac{DU}{\eta} \\ &by\ varying && b,\quad c \\ &subject\ to && 2.5\,\sigma_{max} - \frac{\sigma_{yield}}{1.5} \le 0 \\ & && \sigma_{yield} = 200\ MPa \\ & && b,\ c > 0 \\ & && A = b \cdot c\ > 0 \end{aligned}$$

The required power of the aircraft is optimized by varying both the wingspan and chord of the rectangular wings (with a taper ratio of 1). The bending stress constraint ensures that the wing's structural integrity matches the safety requirement of the design, limiting its maximum value below the yield stress. The projected span and chord (whose product is wing area) constraints ensure the configuration is physically feasible and stays within a bounding platform.

The initial guess of the shape has a 40-meter wingspan and a 2-meter chord as a starting point of the optimization. In the meantime, because there are both aerodynamic and structural considerations in this problem, the resulting wing has a constrained and practical wing aspect ratio for real-world applications. Therefore, this emphasizes the importance of carefully selecting the objective and including all relevant constraints. The parameters for this problem are given in Table 5 as follows:

Table 5: Parameter Values and Descriptions

Parameter	Value	Unit	Description
P	1.2	kg/m^3	Density of air
μ	1.8×10^{-5}	kg/(m sec)	Viscosity of air
k	1.2	–	Form factor
C_L	0.4	–	Lift coefficient
e	0.80	–	Oswald efficiency factor
W_0	1,000	N	Fixed aircraft weight
W_{area}	8.0	N/m^2	Wing area dependent weight
η_{max}	0.8	–	Peak propulsive efficiency
U	20.0	m/s	Flight speed at peak propulsive efficiency
σ_{std}	5.0	m/s	Standard deviation of efficiency function

5. Design Optimization Results

This study presents two sets of numerical results for aircraft wing design optimization: (1) unconstrained optimization and (2) bending stress-constrained optimization. These results were obtained using a validated gradient-based optimizer, employing the BFGS direction search method coupled with a Bracketing line search algorithm. The optimization path and

ISSN: 2790-5209 Vol 3, No.1, 2025
the convergence of relative error are illustrated in Figures 5and 6, validating the robustness of the obtained solutions. The analysis focuses on the optimization results for wingspan, chord, and the required minimum power under varying pressure levels. Additionally, the optimized wing dimensions across different atmospheric conditions are examined, highlighting the relationship between wing area design and environmental factors, as presented in Tables 6 and 7. The findings underscore the optimizer's capability to adapt aircraft wing designs to varying air densities and altitudes, minimizing power requirements based on operational conditions. These results have potential applications, including the design of propeller blades for Martian rotorcraft, where atmospheric conditions differ significantly from Earth's.

5.1. Numerical Solution of Unconstrained Wing Design Optimization

Table 6 presents the results of unconstrained optimization under varying atmospheric conditions, detailing the optimized wing dimensions (span and chord) and the corresponding minimized power. Figure 5 illustrates the optimization path and convergence rate for the wing design process at different pressure levels (740, 300, and 50 torr). These numerical results highlight the performance of the optimizer and provide valuable insights into the optimal wing design configuration under unconstrained conditions.

According to Table 6, it indicates that the wing area design is inversely proportional to pressure levels, as lower atmospheric densities (e.g., at a 30-km altitude) necessitate a significant increase in wing area to generate sufficient lift per unit area. Specifically, both wingspan and chord exhibit exponential growth as air density decreases. Consequently, the minimum required power also increases to account for the additional aerodynamic drag and energy consumption associated with the larger wing area. Under such low-density atmospheric conditions, continuous increases in wing area demand not only a focus on aerodynamic performance but also consideration of aero-structural constraints to ensure a practical and feasible design. To address this, a bending stress-constrained wing design optimization will be analyzed and discussed in the subsequent section.

Theoretically, drag on the wing is directly related to power, which serves as the primary objective in the design optimization, while lift, influenced by air-stream velocity, is indirectly related through the power equation. Consequently, the aerodynamic performance of the aircraft plays a critical role in determining the required power. As indicated by the numerical results in Table 6, a larger wing area—achieved by increasing both wingspan and chord—is essential to sustain flight in rarefied atmospheric conditions. The reduced air density at high altitudes necessitates a proportional increase in wing area to maintain the desired lift. Moreover, the wing area must scale exponentially in such environments due to a substantial decline in the lift coefficient, which directly affects the aerodynamic performance. This increase in wing area compensates for the diminished lift per unit area under rarefied conditions. However, while an enlarged wing area addresses the issue of insufficient lift generation, it introduces significant challenges in terms of structural feasibility. The excessive wingspan and chord dimensions in the unconstrained case could compromise the wing's structural integrity, particularly under bending and shearing stresses during flight. These factors make such designs impractical for real-world applications. Structural constraints, including bending and shearing stress considerations, must be incorporated into the optimization process to address these limitations. This ensures the resulting design not only meets aerodynamic performance requirements but also maintains structural reliability, better reflecting practical application scenarios. Details on the bending stress constraint and its numerical results are provided in Section 5.2.

Table 6: Unconstrained Optimization Results Under Different Atmospheric Conditions

Pressure (Torr)	Air Density (kg/m^3)	Power (W)	Span (m)	Chord (m)	Iteration
740	1.200	923.2824	25.4804	0.5034	15
500	0.769	1014.0571	31.8945	0.6528	19
300	0.461	1179.9399	41.9636	0.8910	23
100	0.154	2503.6149	84.5363	1.8846	41
50	0.077	11216.2987	145.1423	3.2235	52
25	0.038	916587.6889	255.0901	5.3775	12

Table 7: Constrained Optimization Results for Alternative Atmospheric Conditions

Pressure (Torr)	Air Density (kg/m^3)	Power (W)	Span (m)	Chord (m)	Iteration
740	1.200	968.3909	16.6938	0.7772	53
500	0.769	1045.2288	22.5726	0.9298	54
300	0.461	1200.4345	32.0999	1.1702	55
100	0.154	2524.2902	69.7105	2.2791	55
50	0.077	11391.7601	111.3397	4.1370	50
25	0.038	953194.4367	165.7730	7.9020	51

5.2. Numerical Solution of Constrained Wing Design Optimization

Table 7 presents the results of constrained optimization under varying atmospheric conditions, detailing the optimized wing dimensions (span and chord) and the corresponding minimized power with a bending stress constraint function involved. By providing a design bound, this constraint function constrains the wing area within a region where the aero-structural feasibility is. Figure 6illustrates the optimization path and convergence rate for the wing design process at different pressure levels (740, 300, and 50 torr) with a maximum bending stress constraint included (as shown in Equation 14). These numerical results highlight the optimizer's performance and provide valuable insights into the optimal wing design configuration under aero-structural constrained conditions. Comparing the aero-structural constrained optimal designs to the non-constrained ones under varying atmospheric conditions, a more comprehensive necessity of constraints in the design optimization can be represented. Those constraint functions make the optimal design of the objective more reasonable, approaching the situation of applications in real life.

As shown in Table 7, which aligns closely with Table 6, the wing area design remains inversely proportional to pressure levels. At lower atmospheric densities, such as those encountered at a 30-km altitude, the wing area must increase significantly to generate sufficient lift due to the reduced air density. Yet, unlike the unconstrained results, the constrained optimization demonstrates a notable reduction in wingspan and a widening of the chord length. This shift results from the addition of the bending stress constraint, which prevents the wing dimensions from exceeding structural limits. While the unconstrained design prioritizes aerodynamic efficiency with extended wingspans, the constrained design accounts for aero-structural challenges, ensuring that the wing remains feasible under real-world conditions.

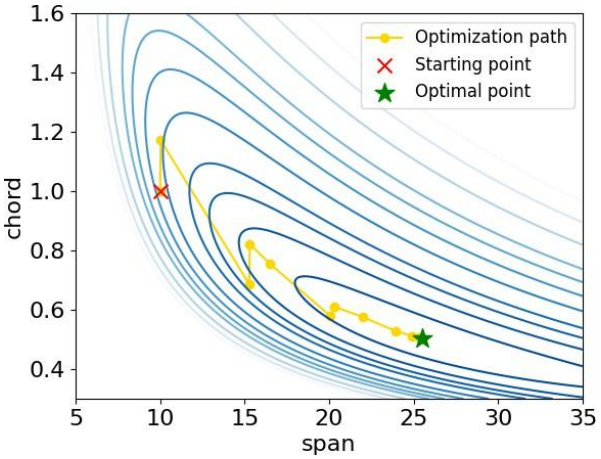

(a) Optimization at 740-torr pressure

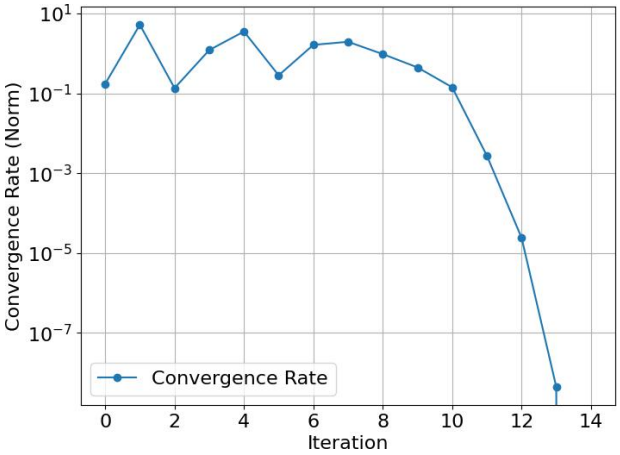

(b) Norm at 740-torr pressure

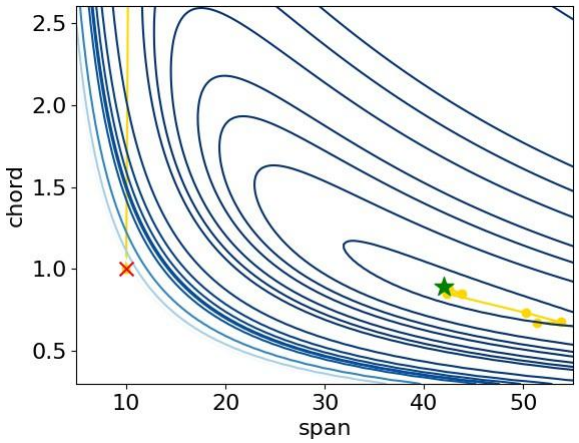

(c)Optimization at 300-torr pressure

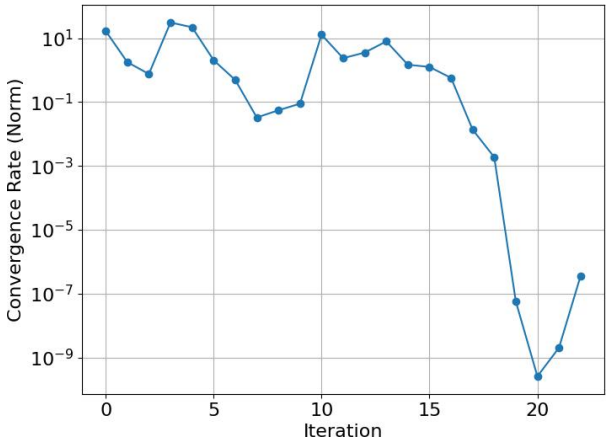

(d) Norm at 300-torr pressure

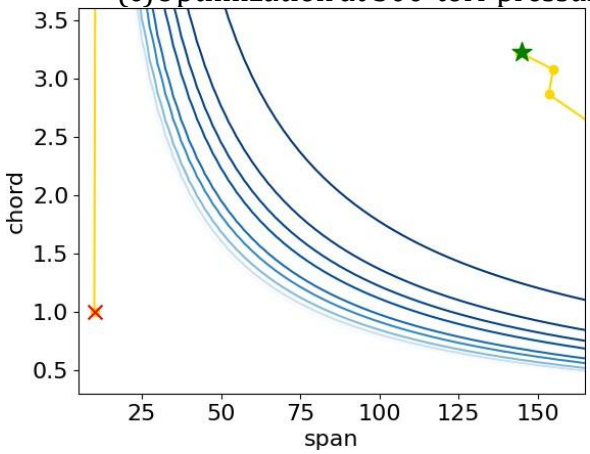

(e) Optimization at 50-torr pressure

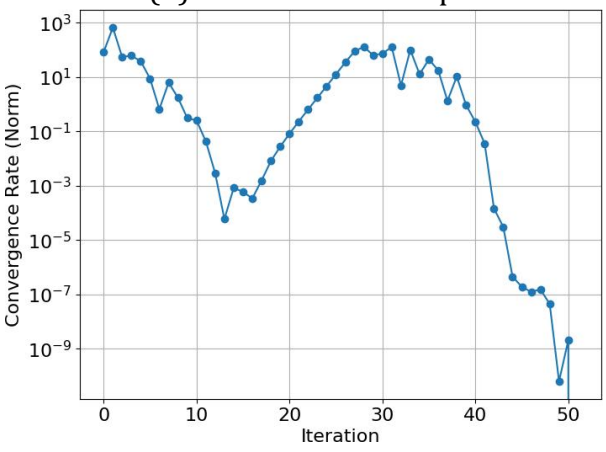

(f) Norm at 50-torr pressure

Fig. 5: Unconstrained aircraft wing design optimization under various atmospheric conditions. Optimization paths and convergence rates are plotted at 740-, 300- and 50-torr pressure levels, respectively.

ISSN: 2790-5209 Vol 3, No.1, 2025

The inclusion of the bending stress constraint leads to several notable trends. As shown in Table 8, the wingspan is reduced by an average of 40%, with decreases ranging from -21.3% at 100 Torr to as much as -53.9% at 25 Torr. These reductions reflect the structural limitations imposed under extreme atmospheric conditions, where an excessively long wingspan would compromise the wing's integrity. In response to the reduced wingspan, the chord length increases to compensate and maintain the required lift. The chord grows by an average of 27%, peaking at 35.2% for 740 Torr and remaining significant at lower pressures, such as 23.9% at 300 Torr and 22.1% at 50 Torr. This adjustment towards a shorter, wider wing enhances structural stability while still achieving the aerodynamic lift necessary for flight. As depicted in Figure 7, the power requirement also shows a modest increase due to the altered wing geometry. On average, the power consumption increases by 2.5%, with the maximum difference observed at 4.66% for 740 Torr and a minimum of 1.54% at 50 Torr. The increase in power arises from aerodynamic inefficiencies introduced by the larger chord and reduced wingspan, which together increase the induced drag. While this increase is relatively small, it highlights the trade-offs inherent in balancing aerodynamic performance and structural constraints. The visual trends presented in Figure 7 further illustrate the impact of the bending stress constraint across different pressure levels. At higher pressures (e.g., 740 Torr), the unconstrained design achieves better aerodynamic efficiency with longer wingspans and narrower chords. However, constrained optimization becomes increasingly critical as the pressure decreases (e.g., 50 Torr and 25 Torr). The results at these lower pressures show a more pronounced reduction in wingspan and an increase in chord length, driven by the need to counteract the extreme decrease in air density while maintaining structural feasibility. Without the bending stress constraint, the unconstrained design would become impractical under such rarefied conditions.

Overall, the constrained optimization strikes a balance between aerodynamic performance and structural integrity. The results demonstrate that while the bending stress constraint slightly increases power consumption, it ensures a feasible wing design with a more realistic geometry. By reducing wingspan and increasing chord length, the constrained design addresses both the aerodynamic and structural challenges posed by varying atmospheric conditions, making it a more practical solution for real-world applications, particularly under low-density environments.

5.3. Optimal Aircraft Wing Design Solutions

Figure 8 provides an overview of the optimized aircraft wing designs across varying atmospheric conditions, specifically at pressure levels of 740 torr, 300 torr, and 50 torr. The results highlight a clear relationship between air density and the total wing area required to maintain sufficient lift. Under standard atmospheric conditions (740 torr), the optimal wing area is approximately 13 m^2. In this case, the higher air density facilitates sufficient lift generation per unit wing area, minimizing the total wing size required. However, as the atmospheric density decreases, the wing area must increase proportionally to compensate for the reduced lift generation caused by insufficient air density and a corresponding reduction in the C_L under rarefied conditions. For example, at 300 torr, the optimal wing area increases to approximately 38 m^2, representing an increase of nearly 192% compared to the standard atmospheric condition. In extremely rarefied conditions, such as at 50 torr, the optimization results yield a significantly larger wing area of approximately 461 m^2. This increase corresponds to a remarkable growth of nearly 35 times (or 3446%) relative to the standard atmospheric environment. Such a dramatic expansion in wing area is essential to generate adequate lift to sustain the aircraft in flight under low-density atmospheric conditions.

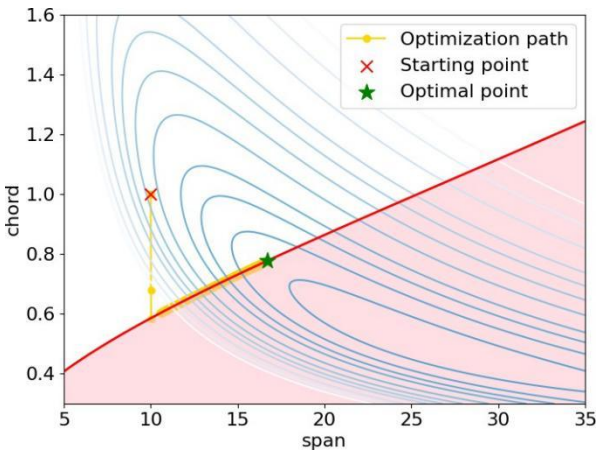

(a) Optimization at 740-torr pressure

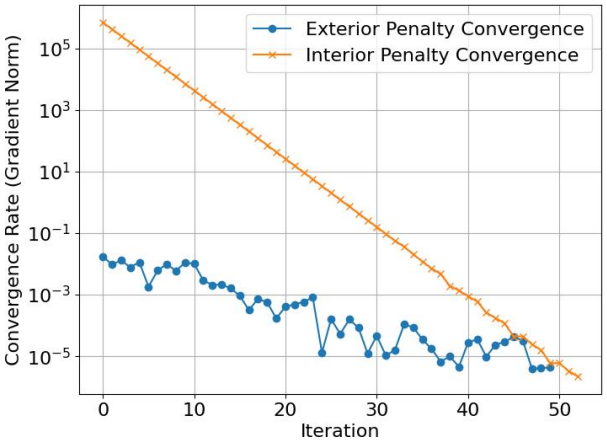

(b) Norm at 740-torr pressure

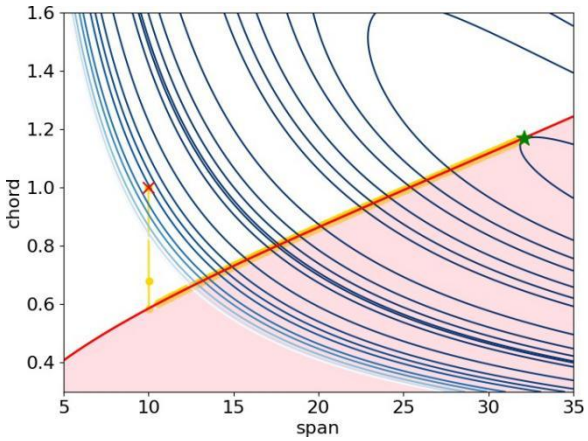

Optimization at 300-torr pressure

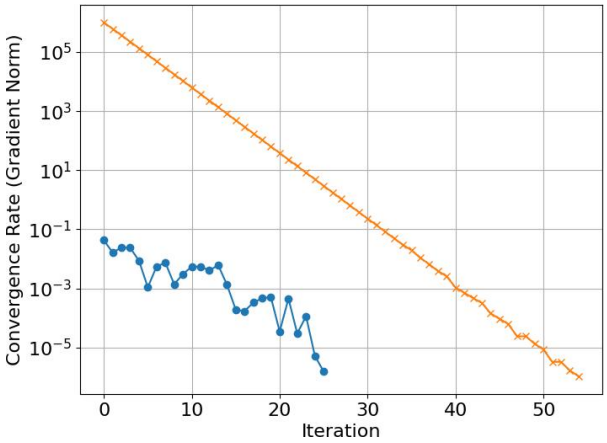

(d) Norm at 300-torr pressure

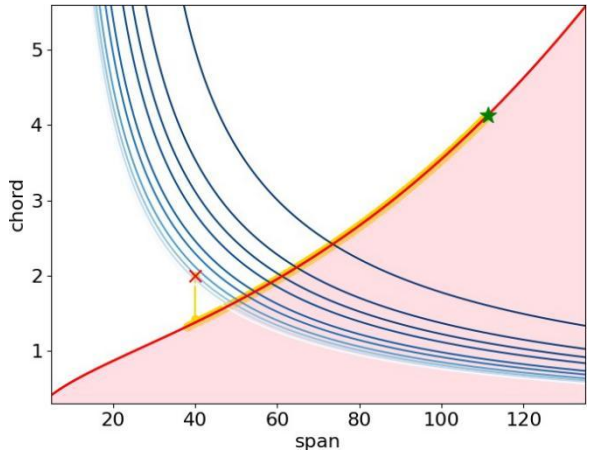

(e) Optimization at 50-torr pressure

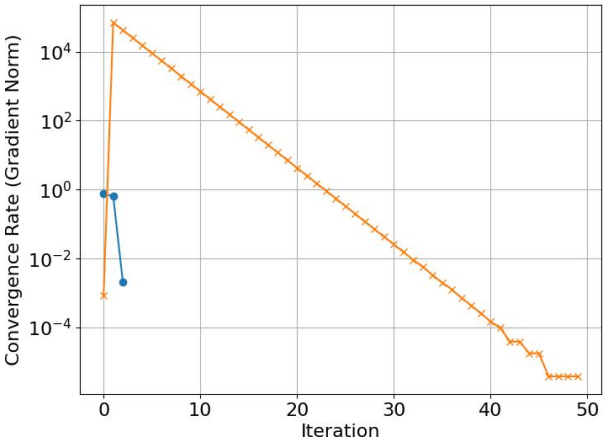

(f) Norm at 50-torr pressure

Fig. 6: Bending stress constrained aircraft wing design optimization under various atmospheric conditions. Optimization paths and convergence rates are plotted at 740-, 300- and 50-torr pressure levels, respectively.

Table 8: Difference in Power, Span, and Chord Across Atmospheric Conditions

Pressure (Torr)	Air Density (kg/m^3)	Power (%)	Span (%)	Chord (%)
740	1.2	4.658091854	-52.633	35.233
500	0.769	2.982283599	-41.297	29.793
300	0.461	1.707260603	-30.728	23.856
100	0.154	0.819056786	-21.268	17.307
50	0.077	1.540248506	-30.360	22.082
25	0.038	3.840428175	-53.879	31.948

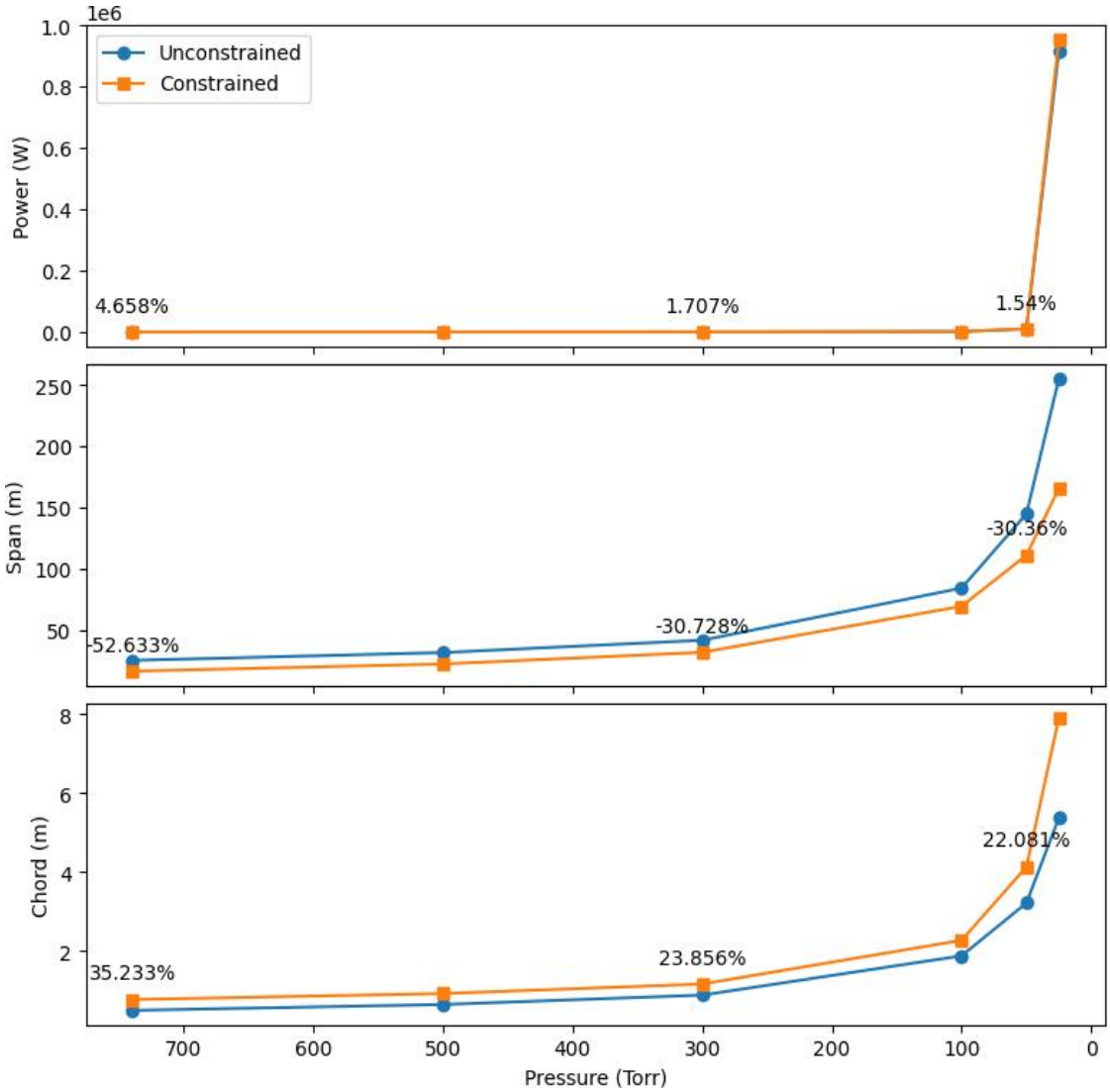

Fig. 7: Percentage of difference in power, wingspan, and chord with pressure levels for the results with and without constraints.

The constrained and unconstrained optimization results exhibit significant differences, underscoring the importance of incorporating aero-structural constraints. By comparing the numerical results with and without the bending stress constraint, it is evident that the constrained optimal design consistently features a shorter wingspan and a wider chord. These

adjustments ensure the design remains within a feasible region that balances aerodynamic efficiency and structural integrity. However, additional constraints should be integrated into the optimizer to enhance the practicality of the wing design further. For example, although the current constrained solution at the 50-torr pressure level achieves structural feasibility, its manufacturability requires further analysis due to the extreme wing dimensions. Additionally, the feasibility of the design during the take-off stage must be considered, particularly in higher air density environments. The large wing area optimized for rarefied conditions could produce excessive lift in dense atmospheric conditions, leading to structural or operational challenges. As a result, such designs may primarily be suited for specialized applications, such as planetary exploration, where the aircraft is deployed in rarefied environments and carried to altitude via a rocket or similar launch vehicle. Expanding the optimization framework to address these considerations will improve the robustness and applicability of the resulting wing designs.

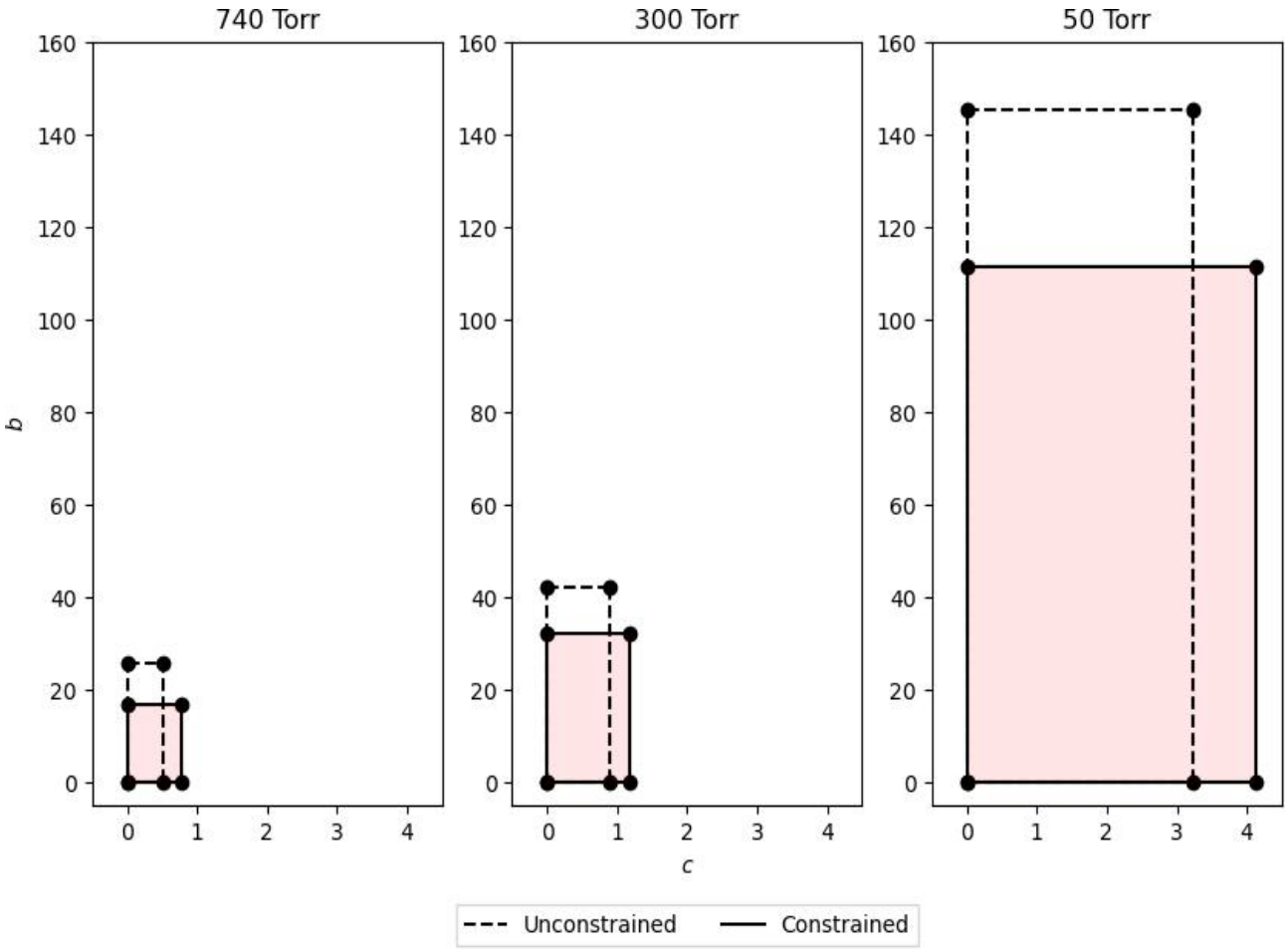

Fig. 8: Overview of the aircraft wing design optimization under varying atmospheric conditions.

6. Future Improvement and Application

Several key enhancements can be considered for future applications to further refine and enhance the optimization framework for aircraft wing design. These improvements include:

1) Addition of a Shear Stress Constraint: In this study, only a bending stress constraint was incorporated. To address aero-structural integrity more comprehensively, an additional shear

stress constraint should be introduced, particularly at the root of the wing. The wing root often experiences the most significant bending stress and shear stress moments during flight due to combined radial, axial, and normal forces. Neglecting shear stress constraints may compromise the structural safety of the design, as the interplay between these forces can result in critical stress levels. Including a shear stress constraint function will better capture the combined effects of bending and shear loads, ensuring greater reliability and robustness in the structural design.

2) Inclusion of Airfoil Thickness: This study focused on the optimization of a 2D aircraft wing using the gradient-based BFGS method. Expanding the framework to include the airfoil thickness and transitioning to a 3D wing model will make the optimization more thorough and practical for real-world applications. The inclusion of thickness enables a better representation of the aerodynamic and structural behaviors of the wing, particularly in complex operational environments.

3) Implementation of the MACH-Aero Framework for Airfoil Optimization: Coupling the current optimization framework with the MACH-Aero platform will provide a more robust aerodynamic shape optimization process for airfoil cross-sections. Similar to the objective of the wing optimization in this study, MACH-Aero focuses on minimizing the drag coefficient (C_D) while maintaining a constant lift coefficient (C_L) across varying pressure levels. By integrating MACH-Aero, the optimization can analyze the airfoil's performance in a broader aerodynamic context.

The implementation of the MACH-Aero framework introduces a gradient-based aerodynamic shape optimization process capable of comparing optimized airfoil designs to existing supercritical airfoils. The minimum-drag airfoils can be obtained using ADFlow, a computational fluid dynamics (CFD) solver integrated into MACH-Aero. The optimization problem is formulated as follows:

- **Objective Function:** Minimize C_D.
- **Equality Constraints:** Maintain C_L, pressure levels, and freestream Mach number.
- **Inequality Constraints:** Restrict the angle of attack (*AOA*), cross-sectional area, chord length, and airfoil thickness.

The goal will be to reduce the drag coefficient at a freestream Mach number below 0.9 while maintaining the desired lift coefficient within a 5-degree corrected AOA (wind tunnel conditions).

The Reynolds number, ranging between 10^4 and 2.5×10^5, will be parameterized concerning the cross-sectional area and angle of attack constraints. The governing equations applied for this optimization will be the 2D Reynolds-Averaged Navier-Stokes (RANS) equations, assuming a constant ratio of specific heats (1.4) and a Prandtl number of 0.71. The wing geometry will be parameterized using the Free-Form Deformation (FFD) method, which allows for smooth, flexible control of the airfoil shape.

By addressing these improvements—adding shear stress constraints, incorporating airfoil thickness, expanding to 3D models, and integrating MACH-Aero—the optimization framework can deliver a more robust, accurate, and practical solution. This will ensure enhanced aerodynamic performance, minimized drag, and greater structural integrity for advanced aircraft designs operating under varying atmospheric conditions.

7. Conclusions

This study presented an optimization framework for aircraft wing design under varying atmospheric conditions, incorporating both aerodynamic and structural considerations within a Multidisciplinary Design Optimization (MDO) approach. The optimization problem was addressed using a gradient-based BFGS method coupled with a Backtracking line search algorithm, which demonstrated superior efficiency, accuracy, and robustness compared to alternative methods.

The numerical results yielded several key findings:

1) **Effect of Atmospheric Conditions on Wing Design:** The wing area design was found to be inversely proportional to atmospheric pressure levels. At standard atmospheric conditions, a relatively small wing area was sufficient due to higher air density facilitating lift generation. However, as the air density decreased, the wing area had to increase significantly to maintain sufficient lift, reflecting the extreme lift requirements under rarefied conditions.

2) **Impact of Structural Constraints on Optimal Design:** The comparison between constrained and unconstrained optimizations highlighted the importance of incorporating aero-structural constraints. Under constrained conditions, the wing designs consistently exhibited shorter wingspans and wider chords compared to the unconstrained results. This trade-off addressed structural feasibility, ensuring that the wing dimensions remained within practical design limits, while maintaining aerodynamic performance.

3) **Power Consumption Trends:** The constrained optimization results showed a modest increase in power requirements, averaging around 2.5%, due to aerodynamic inefficiencies introduced by the altered wing geometry. These findings emphasize the trade-offs between aerodynamic performance and structural integrity when designing wings for extreme environments.

4) **Feasibility of the Optimized Designs:** While the constrained solutions addressed structural limitations effectively, further considerations are necessary for real-world feasibility, particularly during take-off in high-density environments. The large wing areas optimized for rarefied atmospheric conditions may produce excessive lift under standard conditions, posing operational challenges. As such, these designs are best suited for specialized applications, such as planetary exploration, where deployment occurs in low-density atmospheres, and the aircraft is carried to altitude via auxiliary systems like rockets.

In conclusion, this study demonstrated that the BFGS optimization framework, coupled with structural constraints, can effectively adapt wing designs to varying atmospheric conditions while balancing aerodynamic and structural performance. The inclusion of the bending stress constraint ensured practical and feasible designs, particularly under extremely low-density environments. Future improvements, such as incorporating shear stress constraints, airfoil thickness, and 3D optimization, will further enhance the robustness and applicability of the framework. Additionally, integrating the MACH-Aero framework for airfoil optimization will enable the design of minimum-drag airfoils, providing a more comprehensive aerodynamic optimization tool. These advancements will expand the capability of the framework to address complex, real-world aerospace challenges.

Appendix

The 2D Rosenbrock function (shown in Equation 15) was used to test the BFGS optimizer for this study.

$$f(x_1, x_2) = (1 - x_1)^2 + 100(x_2 - x_1^2)^2 \tag{15}$$

The high-dimensional Rosenbrock function used for testing is defined in Equation 16. This function investigates the relationship between function iterations and problem dimensions.

$$f(x) = \sum_{i=1}^{n-1} \left[100(x_{i+1} - x_i^2)^2 + (1 - x_i)^2\right] \tag{16}$$

The derived gradient functions for the multidimensional Rosenbrock function are given in Equation 17.

$$\nabla f(x) = \begin{bmatrix} -2 + 2x_1 - 400x_2x_1 + 400x_1^3 \\ 200x_2 - 200x_1^2 - 2 + 2x_2 - 400x_3x_2 + 400x_2^3 \\ \vdots \\ 200x_{n-1} - 200x_{n-2}^2 - 2 + 2x_{n-1} - 400x_nx_{n-1} + 400x_{n-1}^3 \\ 200x_n - 200x_{n-1}^2 \end{bmatrix} \tag{17}$$

Acknowledgments

We would like to thank Professor Joaquim R. R. A. Martins and our GSI Hannah Hajdik for their support this semester, who provided an excellent MDO course in the Winter 2025 term.

References

[1] Martins, J. R. R. A., and Ning, A., Engineering Design Optimization, Cambridge University Press, 2021.

[2] Bowcutt, K. G., "Multidisciplinary Optimization of Airbreathing Hypersonic Vehicles," Journal of Propulsion and Power, Vol. 17, No. 6, 2001, pp. 1184–1190. https://doi.org/10.2514/2.5893, URL https://doi.org/10.2514/2.5893.

[3] Chen, Y., Hazarika, M. B., Bates, B., and Gamba, M., "Slip Effect Correction for Propeller Blade on Martian Rotorcraft at Rarefied Atmospheric Conditions," AIAA SciTech 2025, American Institute of Aeronautics and Astronautics, 2025. https://doi.org/10.2514/6.2025-0018.

[4] DESERT, T., MOSCHETTA, J.-M., and BEZARD, H., "Aerodynamic Design on a Martian Micro Air Vehicle," 2017. https://doi.org/10.13009/EUCASS2017-365, URL https://www.eucass.eu/doi/EUCASS2017-365.pdf.

[5] Caros, L., Buxton, O., and Vincent, P., "Optimization of triangular airfoils for martian helicopters using direct numerical simulations," AIAA Journal, Vol. 61, No. 11, 2023, p. 4935–4945. https://doi.org/10.2514/1.j063164.

[6] Shapiro, R., and Manela, A., "Thin-airfoil aerodynamics in a rarefied gas wind tunnel: A theoretical study," Physics of Fluids, Vol. 36, No. 5, 2024. https://doi.org/10.1063/5.0203773.

[7] Raymer, D. P., Aircraft Design: A Conceptual Approach, American Institute of Aeronautics and Astronautics, 2018. https://doi.org/10.2514/4.104909.